

LETTER TO THE EDITOR

Heavy Black-Holes Also Matter in Standard Siren Cosmology

Grégoire Pierra¹  and Alexander Papadopoulos² 

¹ INFN, Sezione di Roma, 1-00185 Roma, Italy
 e-mail: gregoire.pierra@roma1.infn.it

² SUPA, University of Glasgow, Glasgow, G12 8QQ, United Kingdom
 e-mail: a.papadopoulos.1@research.gla.ac.uk

ABSTRACT

With the recent release of the largest gravitational-wave (GW) catalog to date—the Gravitational-Wave Transient Catalog (GWTC-4.0) by the LIGO-Virgo-KAGRA (LVK) collaboration—a total of 218 candidate detections of GWs from compact binary coalescences (CBCs) have been reported. This milestone represents a significant advancement for GW cosmology, as most methods, particularly those employing the spectral siren approach, critically depend on the number of available sources. We investigate the impact of a novel parametric model to describe the full population mass spectrum of CBCs, on the estimation of the Hubble constant. This model is specially built to test the impact of heavy black holes in GW cosmology. Our results are compared with the recent measurements reported by the LVK collaboration. We perform a joint inference of cosmological and population parameters using 142 CBCs from GWTC-4.0 with an false alarm rate smaller than 0.25 per year, using both spectral and dark siren approaches. With the spectral sirens, we estimate the Hubble constant to be $H_0 = 78.8_{-15.3}^{+19.0} \text{ km s}^{-1} \text{ Mpc}^{-1}$ (at 68% CL), while the dark siren method yields $H_0 = 82.5_{-14.3}^{+16.8} \text{ km s}^{-1} \text{ Mpc}^{-1}$ (at 68% CL). These results represent improvements of approximately 30.4% and 36.2% in uncertainty, respectively. Furthermore, we demonstrate that this improvement is closely linked to the presence of an new additional mass scale for cosmology in the binary black hole (BBH) mass spectrum, found at $63.3_{-4.8}^{+4.8} M_\odot$. The inclusion of a new mass scale in the BH mass spectrum introduces additional constraints on the estimation of the Hubble constant, yielding precision comparable to that achieved by the two established mass scales at lower masses. Besides providing the tightest constraints on H_0 with standard sirens, it shows the importance of a new heavy mass feature in the BH spectrum.

Key words. gravitational-waves – cosmology – standard sirens – mass scale – GWTC-4.0

1. Introduction

Gravitational-wave (GW) signals from compact binary coalescence (CBCs) offer an independent method for tests of cosmological parameters, most notably the Hubble constant (H_0) Moresco et al. (2022); Pierra & Mastrogiovanni (2025). Since September 2015 the LIGO-Virgo-KAGRA Collaboration (LVK) has detected more than 200 GW events, up to the most recent GWTC-4.0 Abbott et al. (2016); Abac et al. (2025e). These signals provide a direct measurement of the luminosity distance (d_L) and redshifted mass of their source Abac et al. (2025e).

To constrain H_0 with GWs, a redshift value for the source is required. Several methods have been explored to obtain this, including correlation between the sky location of GW events with galaxy catalogs (the “dark siren” method) Palmese et al. (2020); Gray et al. (2022); Mastrogiovanni et al. (2023), or by directly extracting redshift information from an electromagnetic counterpart (the bright siren method) Abbott et al. (2017). The redshift can also be obtained without any external EM information, using the relationship between the detected and source frame mass spectrum, $m_{\text{det}} = (1+z)m_{\text{src}}$. This is known as the “spectral siren” method, providing a fully self-contained inference that requires no EM follow-up or host galaxy identification. Taylor et al. (2012); Ezquiaga & Holz (2022). However it is also essential that the assumed shape of the mass spectrum mirrors the true distribution in order to avoid potential biases Pierra et al. (2024b). Some recent works have also explored the use of non-parametric models for the mass distribution Farah et al. (2025); Tagliazucchi et al. (2025) or even for the Hubble parameter to

avoid potential biases coming from the choice of the parametric model Pierra et al. (2025).

Given that accurate modeling of the CBC mass spectrum is integral to the spectral siren method, the parametric structure of our models should reflect the key features expected in the CBC population. In particular, widely used distributions include a mass gap between neutron stars (NSs) and black holes (BHs) Farr et al. (2011), over-densities associated with pulsational-pair instability supernovae and stable mass-transfer channels in isolated binary evolution Callister & Farr (2024); Godfrey et al. (2024), and possible high-mass excesses arising from hierarchical mergers in dense environments Kimball et al. (2021); Tiwari (2025). Each of these features has the potential to improve GW-based constraints on H_0 . According to the recent LVK analysis, the most robust mass features are a non-empty NS–BH mass gap, an excess around $\sim 10 M_\odot$ and $\sim 35 M_\odot$, and a change in the power-law slope near $\sim 35 M_\odot$.

In this letter, we analyze the GWTC-4.0 catalog using 142 confident CBC detections and a new mass model that includes an additional mass feature for heavy BHs. In Section. 2, we demonstrate how this model translates to an improved estimation of the Hubble constant relative to the fiducial LVK analysis of GWTC-4.0. We examine the impact of this new mass scale on the inferred astrophysical CBC population and on the standard siren measurement. In Section. 3, we discuss the constraining power of such high mass feature with respect to the other mass scales and the intrinsic reason with heavy BHs are crucial in standard siren analysis. Finally, we conclude in Section. 4.

2. Results

Our results are produced using 142 CBCs from the GWTC-4.0 catalog, selected using a FAR < 0.25 yrs Abac et al. (2025e). We compare the results obtained with our new population model with the LVK multi-population model, looking at both spectral and dark siren inferences Abac et al. (2025b). For the dark siren approach, we consider the K-band of the GLADE+ galaxy catalog, with non-uniform luminosity weights Dálya et al. (2018, 2022). To estimate the selection effect, we use the publicly available injection campaign from LVK associated to GWTC-4.0 Abac et al. (2025c); Essick et al. (2025). Details of the inference and the population model are provided in Appendix A. All our results and numerical values are stated as the maximum a posteriori (MAP) value along with the 68% credible level (C.L.) unless otherwise stated.

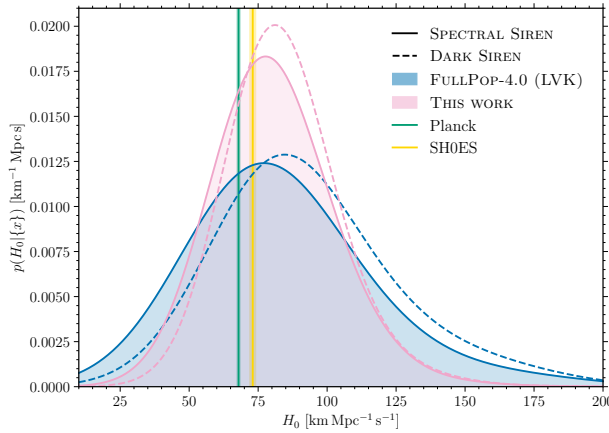


Fig. 1. Marginalized Hubble constant posteriors for different analyses. The fiducial GWTC-4.0 model with FULLPOP-4.0 mass model is shown in blue, and this work shown in pink. The solid lines with filled curves present the spectral siren posteriors, with the dark siren posteriors presented with the dashed lines. Vertical lines are the Hubble tension reference values from Planck and SHOES Ade et al. (2016); Riess et al. (2022).

2.1. The Hubble constant

Figure 1 shows the marginalized posteriors of the Hubble constant obtained with spectral and dark sirens, using our new mass model and comparing to LVK’s multi-population model. We also indicate the recent reference values defining the Hubble tension from Planck and SHOES Ade et al. (2016); Riess et al. (2022). Analyses with our new mass model yield a posterior of $H_0 = 78.8^{+19.0}_{-15.3} \text{ km s}^{-1} \text{ Mpc}^{-1}$ in the spectral siren case, improving to $H_0 = 82.5^{+16.8}_{-14.3} \text{ km s}^{-1} \text{ Mpc}^{-1}$ in the dark siren case. This corresponds to a 30.4% (36.2%) improvement in the Hubble constant constraint for the spectral (dark) siren analysis. This notable improvement is closely linked to the reconstruction of a new mass scale at high masses, which we discuss in Section 2.2. Combining the constraints from our model with the bright siren GW170817 gives $H_0 = 75.4^{+12.6}_{-8.9} \text{ km s}^{-1} \text{ Mpc}^{-1}$ ($H_0 = 77.0^{+12.4}_{-9.4} \text{ km s}^{-1} \text{ Mpc}^{-1}$) for the spectral (dark) siren case, corresponding to an 10.8% (12.9%) improvement relative to LVK’s latest result.

While this parametric model improves the GWTC-4.0 measurement of the Hubble constant, it is still insufficient to resolve the Hubble tension.

Table 1. Table of metrics for comparing the effect of peaks on H_0 estimation, including the 1σ contour of the 2D posterior areas in $[\text{km s}^{-1} \text{ Mpc}^{-1} M_\odot]$ (first column) and axis ratios (second column). These assume the posteriors are approximately gaussian, and include 1σ numerical errors

Model	$A(H_0, \mu_i)$	$r(H_0, \mu_i)$
FULLPOP-4.0 (LVK)	$\mu_1: 104.9 \pm 18.5$	$\mu_1: 0.156 \pm 0.022$
	$\mu_2: 659.8 \pm 16.1$	$\mu_2: 0.136 \pm 0.004$
This work	$\mu_1: 55.8 \pm 9.9$	$\mu_1: 0.184 \pm 0.024$
	$\mu_2: 296.4 \pm 7.8$	$\mu_2: 0.641 \pm 0.044$
	$\mu_3: 469.2 \pm 36.3$	$\mu_3: 0.245 \pm 0.017$

2.2. The heavy black-hole mass scale

As shown in the previous section, introducing an additional mass scale into the BH mass spectrum leads to a tighter constraint on H_0 . We now turn to quantifying the extent of this improvement.

The comparison between the reconstructed mass distributions obtained from the spectral and dark siren inferences (and using both population models) shows very good overall agreement across the full mass range. In particular, both approaches yield consistent results in the NS regime and in the low-mass BH region below $50 M_\odot$. Although, at higher masses, the inferred distributions with our new model indicate an excess of BH around $\sim 63 M_\odot$, not present with the FULLPOP-4.0 model. The reconstructed mass spectra, together with the corresponding discussion of the mass model flexibility and prior choices, are presented in Appendix B (see Fig. B.1).

The impact of this high-mass scale is illustrated in Fig. 2, which shows the correlations between each mass feature and the Hubble constant obtained from the dark siren inference. The spectral siren results are not shown on this figure, but are fully consistent with the dark siren ones. From Fig. 2, we first observe that the additional mass feature is located exactly at $63.3^{+4.8}_{-4.8} M_\odot$ (not overlapping with the other two features), and it exhibits a strong anti-correlation with H_0 . This anti-correlation behavior was anticipated, as previous studies have highlighted the role of mass scales in standard siren inference Abbott et al. (2023); Pierra et al. (2024b); Abac et al. (2025b). Secondly, comparing with the FULLPOP-4.0 model, we see a tightening of the constraints on the means of the other two mass features at lower masses, while their locations remain consistent. Specifically, we find the first mass scale at $8.8^{+0.4}_{-0.5} M_\odot$ and the second at $23.2^{+2.4}_{-3.5} M_\odot$. Although the first two mass scales are better constrained, they still show a strong correlation with the Hubble constant. In other words, the reconstruction of a new mass feature at high masses also better constrains the inferred mass spectrum at lower masses, hence also improving the Hubble constant estimation. We note that in terms of relative weights inferred in each Gaussian peak, we find that the probability in the lower and middle mass peaks dominated compared to that in the high-mass peak, with less than 5% of the total probability contained in the $63 M_\odot$ component.

We verify this effect by quantifying the correlations with H_0 , using the metrics shown in Table 1, based on the 2D posterior areas and axis ratios computed from the covariance matrix (assuming approximately Gaussian posteriors). The 2D area reflects how tightly each mass scale is constrained with H_0 , while the axis ratio serves as a proxy for the strength of their correlation. With the inclusion of a third mass scale, both μ_1 and μ_2 show a substantial reduction in area, from 104.9 to 55.8 and

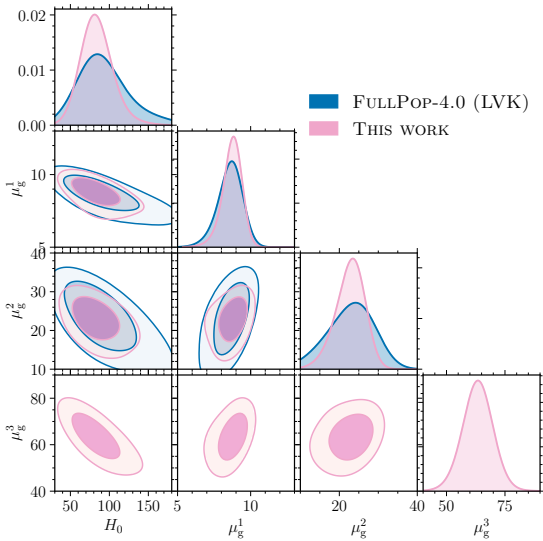


Fig. 2. Inferred 1D posteriors and 2D-contours of the Hubble constant H_0 and the position of the different mass scales, for both the FULLPop-4.0 (blue) and our mass model (pink). The results were obtained with the dark siren inference. The contours shows the 1σ and 2σ levels.

from 659.8 to 296.4 (in $\text{km s}^{-1} \text{Mpc}^{-1} M_\odot$), respectively. The axis ratios reveal that μ_g^1 weakens its degeneracy with H_0 (from 0.156 to 0.184), the same is true of μ_g^2 - changing from 0.136 to 0.641. The new mass scale exhibits a larger posterior area, $469.2 \text{ km s}^{-1} \text{Mpc}^{-1} M_\odot$, and an axis ratio of 0.245, indicating an additional degeneracy with H_0 . However, its main impact is to redistribute the correlations: it reduces the areas of $A(H_0, \mu_1)$ and $A(H_0, \mu_2)$, while creating a third mass scale. Lastly, we find that our constraint of the maximum BH mass is weakened by the additional peak, whilst still being in agreement with the FULLPop-4.0 constraint.

Finally, we find that our new population model is preferred over the FULLPop-4.0 model used by the LVK, despite its higher dimensionality. As discussed in Abac et al. (2025b), applying narrower priors to both models yields Bayes factors of 6 once reweighted by the effective prior volume.

3. Discussion

Quantifying the contribution of each mass scale to the overall estimation of the Hubble constant is a challenging task. Recent studies have begun to explore this question. For instance, Manarella & Gerosa (2025) investigates the impact of individual GW events on H_0 , while Mali & Essick (2025) examines in detail the correlation between the $30 M_\odot$ and H_0 . Here, rather than focusing on individual events or on deriving correlation coefficients, we aim to understand how the different inferred mass scales contribute to the resulting cosmological constraints. In Pierra et al. (2025), it is explained why the constraining power of the standard siren method arises from the evolution of the mass spectrum (and in particular mass features) when looked in the detector frame, tracked jointly in the $\{d_L, m_{\text{det}}\}$ parameter space. Mass scales that show strong evolution across this space contribute more significantly to the final constraints on the cosmological parameters. Conversely, if the mass spectrum were

constant across all distances, the method would provide little information. Another important factor is how well each scale is constrained, so the most informative mass scales are those that both exhibit strong evolution in the detector frame and are tightly inferred from the GW data.

Figure 3 shows the inferred evolution of the main mass features in the $\{d_L, m_{\text{det}}\}$ parameter space, namely the minimum and maximum masses, and the three Gaussian components of our new population model. This evolution is reconstructed from posterior samples of the mass distribution parameters and H_0 . For each sample, the inferred source-frame mass scales are converted to detector-frame using $m_{\text{det}} = (1+z) m_{\text{src}}$, while the corresponding luminosity distance is computed from the redshift, using the H_0 posterior. This approach allows us to visualize the evolution of the mass scales and their uncertainties in the parameter space relevant to the detected signals. Based on Fig. 3, we can draw the following conclusions: (i) the minimum mass shows no evolution in the $\{d_L, m_{\text{det}}\}$ space, which explains why this mass scale does not usually correlate with H_0 , therefore does not contribute to its constraining power. In contrast, the maximum mass evolves strongly, but its large uncertainties limit its impact, consistent with the typical H_0-m_{max} correlation observed with standard siren Abac et al. (2025b). (ii) All three Gaussian components exhibit some evolution with d_L , with the third peak displaying the strongest. (iii) The first peak, while evolving slightly less than the others, has the smallest uncertainties, hence has equivalent constraining power as the third one. These conclusions are consistent with the metrics derived in Section 2 and demonstrate that the constraining power of a mass scale is governed by the interplay between its evolution in the $\{d_L, m_{\text{det}}\}$ space and how well it can be inferred from the GW data.

As an additional test, we also investigated the inclusion of the special GW candidate GW231123 Abac et al. (2025a). This event, with a total detector-frame mass exceeding $200 M_\odot$, was excluded in the recent LVK cosmology analysis. Since our study focuses on the role of heavier BHs, GW231123 could potentially have an impact here. Re-running all our analyses including this event, we find that the improvement in the Hubble constant constraints decreases to 8.5% and 4% for the dark and spectral approaches, respectively. In particular, we observe that the inclusion of this massive event pushes the inferred maximum mass to $\sim 170 M_\odot$, and that the second and third Gaussian peaks become less well constrained compared to the analysis without this event. This may indicate that even our extended mass model struggles to accommodate such an extreme system within the overall population.

We verified that our results are numerically stable with respect to the evaluation and convergence of the hierarchical Bayesian framework. In particular, we reproduced our analyses using a cut on the variance of the log-likelihood, such that $\text{var}(\log \mathcal{L}) < 1$, which was shown as a reliable threshold in Talbot & Golomb (2023). We find that our results remain in perfect agreement when this threshold is applied.

Besides, our inferred mass spectrum does not exhibit the pronounced feature reported in Magaña Hernandez & Palmese (2025), where their semi-parametric approach indicates an excess around $\sim 75 M_\odot$ followed by a sharp drop before $80 M_\odot$. Such feature is in disagreement with our results, and it also appears to be in tension with their parametric model as well as with other recent studies using both parametric and non-parametric mass models Abac et al. (2025b,d); Tagliazucchi et al. (2025); Tiwari (2025) with GWTC-4.0 data. This discrepancy, seen in both our results and other independent analyses, suggests that the reported excess in Magaña Hernandez & Palmese (2025) is

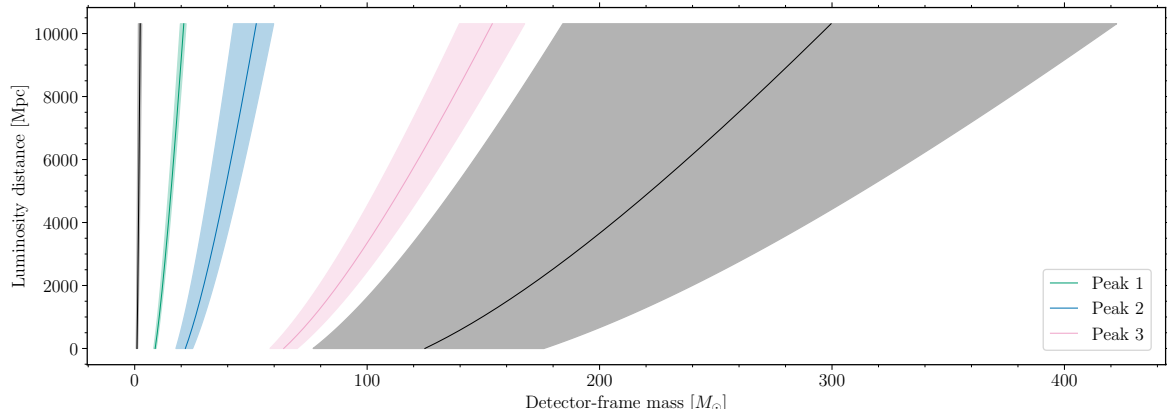


Fig. 3. Mass scale evolution estimated from the dark siren inference of GWTC-4.0, visualized in the detector frame $\{d_L, m_{\text{det}}\}$. The solid lines represent the MAP value of the different mass scales of our population model, namely the minimum and maximum masses (black), the first (green), second (blue) and third (pink) Gaussian peaks. The shaded regions show the 68% C.L.

likely model-induced and therefore their constraints on the Hubble constant are over-estimated.

Finally, the BH excess we find at $63 M_\odot$ might be the signature of a sub-population of BHs. We refer the reader to recent population-focused works Gerosa & Fishbach (2021); Li et al. (2024); Pierra et al. (2024a).

4. Conclusions

In this letter, we have demonstrated that heavy BHs have a strong impact on standard siren cosmology, for both spectral and dark sirens. Specifically, we have shown that the BH mass spectrum exhibits an excess around $63 M_\odot$, and that this feature can be used as a new mass scale in GW cosmology when an adequate population model is employed. We find that the constraint on H_0 improves by 36.2% with 141 dark sirens, relative to the latest LVK result using the GWTC-4.0 catalog. When combined with the bright siren GW170817, the improvement reaches 12.9%, yielding $H_0 = 77.0_{-9.4}^{+12.4} \text{ km s}^{-1} \text{ Mpc}^{-1}$. Moreover, we show that the additional cosmological constraining power provided by our model is not solely due to the new mass scale at $63.3_{-4.8}^{+4.8} M_\odot$, but also to the improved constraints on the two other mass scales around $\sim 9 M_\odot$ and $\sim 23 M_\odot$ triggered by the more precise reconstruction of the high mass region. Finally, we quantify the relative importance of each mass scale for constraining the Hubble constant. In particular, we show that, when examined in the detector-frame plane, the constraining power of a mass scale is determined by the combination of its evolution in that plane and how well it can be measured, making the $63 M_\odot$ scale a newly important one. Future standard-siren analyses should therefore consider models capable of capturing this feature.

Acknowledgements. G. Pierra is supported by ERC grant GravitySirens 101163912. Funded by the European Union. Views and opinions expressed are however those of the author(s) only and do not necessarily reflect those of the European Union or the European Research Council Executive Agency. Neither the European Union nor the granting authority can be held responsible for them. A. Papadopoulos is supported by UKRI STFC studentship 323353-01. A.P thanks Rachel Gray and Chris Messenger for their useful discussions. This material is based upon work supported by NSF's LIGO Laboratory which is a major facility fully funded by the National Science Foundation. The authors are grateful for computational resources provided by the LIGO Laboratory and supported by National Science Foundation Grants PHY-0757058 and PHY-0823459.

References

- Abac, A. G. et al. 2025a, *Astrophys. J. Lett.*, 993, L25
- Abac, A. G. et al. 2025b, [[arXiv:2509.04348](https://arxiv.org/abs/2509.04348)]
- Abac, A. G. et al. 2025c, [[arXiv:2508.18081](https://arxiv.org/abs/2508.18081)]
- Abac, A. G. et al. 2025d, [[arXiv:2508.18083](https://arxiv.org/abs/2508.18083)]
- Abac, A. G. et al. 2025e, [[arXiv:2508.18082](https://arxiv.org/abs/2508.18082)]
- Abbott, B. P., Abbott, R., Abbott, T. D., et al. 2017, *Nature*, 551, 85–88
- Abbott, B. P. et al. 2016, *Living Rev. Rel.*, 19, 1
- Abbott, R. et al. 2023, *Astrophys. J.*, 949, 76
- Ade, P. A. R. et al. 2016, *Astron. Astrophys.*, 594, A13
- Callister, T. A. & Farr, W. M. 2024, *Physical Review X*, 14
- Dálya, G., Gaigóczki, G., Dobos, L., et al. 2018, *Mon. Not. Roy. Astron. Soc.*, 479, 2374
- Dálya, G. et al. 2022, *Mon. Not. Roy. Astron. Soc.*, 514, 1403
- Essick, R. et al. 2025, *Phys. Rev. D*, 112, 102001
- Ezquiaga, J. M. & Holz, D. E. 2022, *Physical Review Letters*, 129
- Farah, A., Fishbach, M., Essick, R., Holz, D. E., & Galaudage, S. 2022, *The Astrophysical Journal*, 931, 108
- Farah, A. M., Callister, T. A., Ezquiaga, J. M., Zevin, M., & Holz, D. E. 2025, *Astrophys. J.*, 978, 153
- Farr, W. M., Sravan, N., Cantrell, A., et al. 2011, *The Astrophysical Journal*, 741, 103
- Fishbach, M., Essick, R., & Holz, D. E. 2020, *The Astrophysical Journal Letters*, 899, L8
- Gerosa, D. & Fishbach, M. 2021, *Nature Astron.*, 5, 749
- Godfrey, J., Edelman, B., & Farr, B. 2024, *Cosmic Cousins: Identification of a Subpopulation of Binary Black Holes Consistent with Isolated Binary Evolution*
- Gray, R., Messenger, C., & Veitch, J. 2022, *Monthly Notices of the Royal Astronomical Society*, 512, 1127–1140
- Kimball, C., Talbot, C., Berry, C. P. L., et al. 2021, *The Astrophysical Journal Letters*, 915, L35
- Kotz, S., Balakrishnan, N., & Johnson, N. L. 2000, *Continuous Multivariate Distributions, Volume 1: Models and Applications*, 2nd edn. (Wiley), 485 – 527
- Li, Y.-J., Wang, Y.-Z., Tang, S.-P., & Fan, Y.-Z. 2024, *Phys. Rev. Lett.*, 133, 051401
- Madau, P. & Dickinson, M. 2014, *Ann. Rev. Astron. Astrophys.*, 52, 415
- Magaña Hernández, I. & Palmese, A. 2025, [[arXiv:2509.03607](https://arxiv.org/abs/2509.03607)]
- Mali, U. & Essick, R. 2025, *Astrophys. J.*, 980, 85
- Mancarella, M. & Gerosa, D. 2025, *Phys. Rev. D*, 111, 103012
- Mandel, I., Farr, W. M., & Gair, J. R. 2019, *Mon. Not. Roy. Astron. Soc.*, 486, 1086
- Mastrogiovanni, S., Laghi, D., Gray, R., et al. 2023, *Phys. Rev. D*, 108, 042002
- Mastrogiovanni, S., Pierra, G., Perriès, S., et al. 2024, *Astron. Astrophys.*, 682, A167
- Moresco, M. et al. 2022, *Living Rev. Rel.*, 25, 6
- Palmese, A., deVicente, J., Pereira, M. E. S., et al. 2020, *The Astrophysical Journal Letters*, 900, L33
- Pierra, G., Colombo, A., & Mastrogiovanni, S. 2025, [[arXiv:2511.11795](https://arxiv.org/abs/2511.11795)]
- Pierra, G. & Mastrogiovanni, S. 2025, [[arXiv:2507.10597](https://arxiv.org/abs/2507.10597)]
- Pierra, G., Mastrogiovanni, S., & Perriès, S. 2024a, *Astron. Astrophys.*, 692, A80
- Pierra, G., Mastrogiovanni, S., Perriès, S., & Mapelli, M. 2024b, *Phys. Rev. D*, 109, 083504
- Riess, A. G. et al. 2022, *Astrophys. J. Lett.*, 934, L7
- Tagliazucchi, M. et al. 2025, *in prep*
- Talbot, C. & Golomb, J. 2023, *Mon. Not. Roy. Astron. Soc.*, 526, 3495
- Taylor, S. R., Gair, J. R., & Mandel, I. 2012, *Physical Review D*, 85
- Tiwari, V. 2025, [[arXiv:2510.25579](https://arxiv.org/abs/2510.25579)]
- Vitale, S., Gerosa, D., Farr, W. M., & Taylor, S. R. 2020, [[arXiv:2007.05579](https://arxiv.org/abs/2007.05579)]

Appendix A: Inference framework

The standard siren method enables the joint inference of the cosmological and population parameters describing the properties of CBCs, using a set of GW candidates. We use the Python package `icarogw`, a hierarchical Bayesian pipeline designed to infer cosmological and population properties from GW data while accounting for selection effects Mastrogiiovanni et al. (2024, 2023). To account for these selection effects—that is, the finite sensitivity of the current LVK detectors—we use the publicly available injection campaign associated with GWTC-4.0. Further details on the construction and use of these injections can be found in Essick et al. (2025); Pierra & Mastrogiiovanni (2025).

Appendix A.1: Hierarchical likelihood

Following Mandel et al. (2019); Vitale et al. (2020); Mastrogiiovanni et al. (2024, 2023), the hierarchical likelihood of observing N_{obs} GW events, given the data set $\{\mathbf{x}\}$, marginalizing over the local CBC merger rate R_0 , can be written as

$$\mathcal{L}(\{\mathbf{x}\}|\Lambda) \propto \prod_{i=1}^{N_{\text{obs}}} \frac{\int d\theta dz \mathcal{L}(\mathbf{x}_i|\theta, z, \Lambda) \frac{1}{1+z} \frac{dN_{\text{cbc}}(\Lambda)}{d\theta dz dt_s}}{\int d\theta dz p_{\text{det}}(\theta, z, \Lambda) \frac{1}{1+z} \frac{dN_{\text{cbc}}(\Lambda)}{d\theta dz dt_s}}, \quad (\text{A.1})$$

where $\mathcal{L}(\mathbf{x}_i|\theta, z, \Lambda)$ is the single-event likelihood, with θ the binary's intrinsic parameters, z the redshift, and Λ the hyperparameters. The denominator captures the selection effects through the probability of detection $p_{\text{det}}(\theta, z, \Lambda)$ estimated with the injection campaign. The population models describing the CBC mass distribution and CBC merger rate enter through the CBC overall rate

$$\frac{N_{\text{cbc}}(\Lambda)}{d\theta dz dt_s} = \mathcal{R}(z|\Lambda) p_{\text{pop}}(\theta|z, \Lambda) \frac{1}{1+z} \frac{dV_c}{dz}, \quad (\text{A.2})$$

where $\mathcal{R}(z|\Lambda)$ is the source-frame rate per comoving volume V_c , chosen to be the commonly used Madau&Dickinson like star formation rate Madau & Dickinson (2014), and $p_{\text{pop}}(\theta|z, \Lambda)$ is the population distribution, here describing solely the CBC mass distribution. This framework follows the approach used in recent GW cosmology analyses with GWTC-4.0 Abac et al. (2025b); Pierra et al. (2025).

Appendix A.2: Population mass model

The new population model used in our analysis builds on the `FULLPOP-4.0` from Abac et al. (2025b), which in turn is an extension of the `POWERLAW-DIP-BREAK` from Fishbach et al. (2020) and Farah et al. (2022). It covers the whole CBC mass range (NSs+BHs) and employs two identical distributions for the primary and secondary masses, combined with a pairing function which ensure $m_1 > m_2$. The basic construction is a broken power-law with two Gaussian peaks, and we develop this by increasing the number of Gaussian peaks to three, such that the mass distribution becomes

$$\begin{aligned} p_{\text{pop}}(m_{1,s}|\Lambda) &= (1 - \lambda_g) \mathcal{B}(m_{1,s}|m_{\text{min}}, m_{\text{max}}, \alpha_1, \alpha_2, b) \\ &+ \lambda_g \lambda_1 \mathcal{G}_1(m_{1,s}|\mu_1, \sigma_1) \\ &+ \lambda_g (1 - \lambda_1) \lambda_2 \mathcal{G}_2(m_{1,s}|\mu_2, \sigma_2) \\ &+ \lambda_g (1 - \lambda_1) (1 - \lambda_2) \mathcal{G}_3(m_{1,s}|\mu_3, \sigma_3), \end{aligned}$$

$$p_{\text{pop}}(m_{2,s}|\Lambda) = p_{\text{pop}}(m_{1,s}|\Lambda). \quad (\text{A.3})$$

Where \mathcal{B} is a broken power-law, \mathcal{G} are the Gaussian components, and the weights between the Gaussian feature and the rest of

the distribution are given by $\lambda_{i \in [1,2]}$. The overall distribution also include a low and high mass tapering to avoid a non-physical sharp cut-off.

To ensure that all Gaussian peaks receive equal prior weight, we place a Dirichlet prior on the mixture weights defined in Eq. A.3. In this framework, we assign a Beta prior ($\alpha = 1, \beta = 2$) to λ_1 and a uniform prior to λ_g and λ_2 , so that the combined peak weights correspond to the elements of a symmetric Dirichlet distribution Kotz et al. (2000).

Appendix B: Reconstructed mass spectra

Figure B.1 shows a comparison of the reconstructed mass distributions obtained from the spectral and dark siren inferences applied to GWTC-4.0, with the `FULLPOP-4.0` model from LVK (blue) and our new model (pink). The two approaches are in very good agreement over the full mass range.

In particular, the reconstructed spectra are consistent in the NS regime and in the low-mass BH region below $50 M_\odot$. In the high-mass region of the distribution, the analyses with our new model reveal an additional accumulation of BH around $\sim 63 M_\odot$, which is visible in Fig. B.1. This feature is recovered consistently by the spectral and dark siren frameworks, indicating that it is not driven by a specific inference methodology.

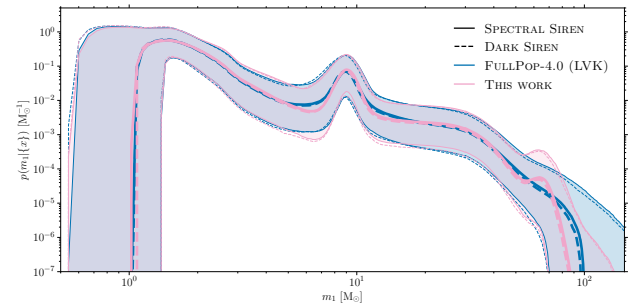


Fig. B.1. Posterior predictive distribution of the primary mass spectrum, with the `FULLPOP-4.0` in blue and our model in pink. The thick lines denote the median shape of the distribution, while the filled regions give the 68% C.L.

The population models employed in this work is designed to be flexible and does not enforce the presence of any mass feature a priori. In particular, the model allows the data to determine whether localized structures, such as peaks, are supported by the observations. To ensure an agnostic inference of possible mass scales, the prior ranges for the means and variances of all Gaussian components span the entire BH mass spectrum, from $5 M_\odot$ to $150 M_\odot$. This choice prevents the artificial introduction of preferred mass scales and ensures that any recovered feature is as much data-driven as possible.